

# The formation mechanism of metastable $\text{Al}_6(\text{Fe}, \text{Mn})$ phase in die-cast Al-Mg alloys

Xiangzhen Zhu<sup>a</sup>, Paul Blake<sup>b</sup>, Shouxun Ji<sup>a\*</sup>

<sup>a</sup> Brunel Centre for Advanced Solidification Technology (BCAST), Brunel University London, Uxbridge, Middlesex UB8 3PH, United Kingdom

<sup>b</sup> Engineering Centre, Jaguar Land Rover, Abbey Road, Coventry, CV34 4LF, United Kingdom

\* Corresponding author: Tel.: +44 1895 266663, Fax: +44 1895 269758, Email: shouxun.ji@brunel.ac.uk

## Abstract

The formation, 3D morphology and growth mechanism of  $\text{Al}_6(\text{Fe}, \text{Mn})$  phase were studied in Al-Mg-Mn-Fe alloys processed by high pressure die casting (HPDC). Thermodynamic calculation indicates  $\text{Al}_6(\text{Fe}, \text{Mn})$  phase in the HPDC Al-Mg-Mn-Fe alloys is a metastable phase. The experimental results confirm that Mn addition in the alloy suppresses the transformation from metastable  $\text{Al}_6(\text{Fe}, \text{Mn})$  phase to stable  $\text{Al}_{13}(\text{Fe}, \text{Mn})_4$  phase under nonequilibrium solidification conditions. Energy-dispersive spectroscopy (EDS) analysis of extracted particles reveals that the average Mn/Fe atomic ratio in the  $\text{Al}_6(\text{Fe}, \text{Mn})$  phase decreases as the Mn/Fe atomic ratio in the melt decreases. It is also found that the  $\text{Al}_6(\text{Fe}, \text{Mn})$  phase grows to form two elongated prism morphologies: rhombic prism (equilibrium morphology, bounded by  $\{110\}$  and  $\{002\}$ ), and rectangular prism (growth morphology, bounded by  $\{002\}$ ,  $\{200\}$  and  $\{020\}$ ). The primary  $\text{Al}_6(\text{Fe}, \text{Mn})$  phase shows hollow structure and the eutectic is in the form of fine solid particles. The growth mechanism of  $\text{Al}_6(\text{Fe}, \text{Mn})$  phase is also elucidated according to the crystallographic rules and the morphological characteristics of  $\text{Al}_6(\text{Fe}, \text{Mn})$  phase.

## Key words:

aluminium alloys; microstructure; crystal growth; metastable phase; 3D morphology

# 1. Introduction

In die-cast aluminium alloys, Fe is a common impurity as it is unavoidably picked up in practice. This is mainly because molten aluminium can dissolve steel tools and processing equipment to increase the Fe content in melt [1, 2]. As so far, there are no economically profitable methods to completely remove the Fe contents from melt. Therefore the accumulation of iron has been a critical concern in die-cast components. This is particularly serious for the application of recycled materials. The excessive Fe is strongly prone to form various long needle-like (in 2D) or plate-like (in 3D) Fe-bearing intermetallic phases [3–5]. These intermetallics are generally brittle and act as stress raisers to weaken the coherence with Al matrix. Consequently, the cast components are degraded in terms of the mechanical properties (elongation, especially)[6]. The detrimental effect of Fe impurity has been an obstacle for the application of recycled aluminium alloys.

In the past several decades, numerous efforts have been made to diminish the detrimental effect of Fe in aluminium alloys. Several methods including melt-superheating treatment, chemical modification (Ca, Sr, Mn), solidification under high cooling rate and non-equilibrium heat treatment have been found to be effective to improve the mechanical properties of Al-Si alloys with increased Fe contents [7]. Of these methods, the addition of Mn is a common method to modify Fe-bearing phases from needle-like  $\beta$ -AlFeSi to blocky  $\alpha$ -AlFeMnSi morphology. However, when overall amount of Mn and Fe is more than 1.5wt.%, depending on the Si contents, there is a sharp increase of the risk to obtain colonies of large primary  $\alpha$ -AlFeMnSi crystals [8]. The morphological change of Fe-bearing phases results in the unacceptable mechanical performance in the cast components.

Unlike the formation of Fe-bearing phases is closely linked with the presence of Si in Al-Si alloys. The Fe-bearing phases formed in other aluminium alloys are different. It has been found that the addition of Mn in **\*\*** alloys can transform  $\text{Al}_3\text{Fe}$  to  $\text{Al}_6(\text{Fe}, \text{Mn})$  [9]. The increased cooling rate can significantly refine the  $\text{Al}_6(\text{Fe}, \text{Mn})$  phase [10]. These can possibly increase the upper limit of Fe level in aluminium alloys. In particular, Fe-bearing phases in aluminium alloys is helpful in improving the yield strength with the scarification of ductility of die-cast aluminium alloys **[ji paper]**. Therefore, if the Fe-bearing phase is properly modified for the required morphology, the detrimental effect on ductility can be minimised.

This will be practically very useful to allow Fe as a beneficial element in aluminium alloys that already has sufficient ductility to be neutralised by Fe element.

Therefore, the morphology of intermetallic phases has a vital effect on the properties of aluminium alloys. However, it is still very limited for the understanding of growth mechanism particularly in the non-silicon aluminium alloys. For example, in Al-Mg-Mn alloys, although the size and amount of  $Al_6(Fe, Mn)$  have been studied at  $Fe < 0.6$  wt.%) under different solidification conditions, the morphology of  $Al_6(Fe, Mn)$  phase and growth mechanism are unclear [10–12]. Because it is desirable to high Fe content as a beneficial element, the study of 3-D morphology and growth mechanism of  $Al_6(Fe, Mn)$  phase is important for technical exploitation. Moreover, the habit planes (i.e. the exposed plane) of  $Al_6(Fe, Mn)$  dispersoids has been the objects of many current studies. However, the observed habit planes are also different [13–15].

The present study aims to reveal the 3-D morphology and growth mechanism of  $Al_6(Fe, Mn)$  in Al-Mg-Mn alloys with different levels of Fe contents. The effect of Fe contents on the microstructure and the formation of  $Al_6(Fe, Mn)$  was studied in the die-cast Al-Mg-Mn alloys under as-cast condition. The discussion focused on the understanding of the precipitation behaviour during solidification.

## **2. Experimental procedures**

Commercial pure Al and Mg ingots, Al-20%Mn and Al-45%Fe master alloys (all compositions quoted in this paper are in wt.% unless otherwise stated) were used to prepare a series of Al-5Mg-xFe-0.6Mn alloys ( $x=0.1, 0.5, 1.0, 1.5$  and  $2.0$ ). Firstly, the starting materials were melted in a clay-graphite crucible using an electric resistance furnace at  $730$  °C. After a homogenization process for about 30min, the melt was manually dosed and subsequently released into the shot sleeve of a 4500 kN cold chamber HPDC machine. The pouring temperature was controlled at  $720$  °C measured by a K-type thermocouple. The die was preheated by the circulation of mineral oil at  $150$ °C in all shots.

The metallographic samples were cut from the middle of round ASTM standard samples with a  $\Phi 6.35$  mm, and then mechanically ground and polished using standard method. In order to observe the 3D morphologies of as-synthesized  $Al_6(Fe, Mn)$  clearly, a 15 vol% HCl–distilled water solution was used to deep-etch or completely remove the matrix of the samples, and then  $Al_6(Fe, Mn)$  particles were collected utilizing a centrifugal extractor by segregating the

solution. The phase identification and microstructure characterization of the samples were carried out using X-ray diffraction (XRD, Rigaku D/max-rB, Japan) and scanning electron microscopy (SEM, Zeiss-Supra 35VP, Germany) equipped with energy-dispersive x-ray spectroscopy (EDS) and electron back-scattered diffraction (EBSD).

### 3. Results and discussion

#### 3.1 Microstructures of Al-Mg-Mn-Fe alloys

Figure 1 shows the microstructures of Al-5Mg-xFe-0.6Mn alloys ( $x=0.5, 1.0, 1.5$  and  $2.0$ ). According to the XRD patterns shown in Figure 2, all bright intermetallic compounds in alloys are identified as  $\text{Al}_6(\text{Fe}, \text{Mn})$  phase. While, the morphology, size and amount of  $\text{Al}_6(\text{Fe}, \text{Mn})$  phase changes obviously as the increase of Fe levels. In the 0.5Fe alloy,  $\text{Al}_6(\text{Fe}, \text{Mn})$  locates at the grain boundary of  $\alpha$ -Al grains and shows a regular eutectic morphology with some curved plane. As the Fe level increases to 1.0%, few primary  $\text{Al}_6(\text{Fe}, \text{Mn})$  phase forms, as shown in Figure 1c. What's more notable, the regular eutectic with alternately distributed  $\alpha$ -Al and  $\text{Al}_6(\text{Fe}, \text{Mn})$  phases disappears. Accordingly, divorced eutectic  $\text{Al}_6(\text{Fe}, \text{Mn})$  phase with faceted plane dominates. The divorced eutectic  $\text{Al}_6(\text{Fe}, \text{Mn})$  phase has two typical morphologies, i.e, needle and small rhombus, as shown in Figure 1d. When Fe level further increases to 1.5% and 2.0%, divorced eutectic  $\text{Al}_6(\text{Fe}, \text{Mn})$  phase is maintained, but the amount and size of primary  $\text{Al}_6(\text{Fe}, \text{Mn})$  phase increase. Similar with the morphologies of divorced eutectic  $\text{Al}_6(\text{Fe}, \text{Mn})$  phase, primary  $\text{Al}_6(\text{Fe}, \text{Mn})$  phase also has lath-like (i.e. coarse needle-like) and rhombic morphologies in two dimensions. It is interesting to note that there exists a hollow in the centre of the rhombic primary  $\text{Al}_6(\text{Fe}, \text{Mn})$  phase.

To observe the morphologies of hollow primary  $\text{Al}_6(\text{Fe}, \text{Mn})$  clearly, samples were deep-etched by a 15 vol.% HCl-distilled water solution. As shown in Figure 3, the hollows have different sizes, shapes and locations. Most hollows are in the centre of rhombic  $\text{Al}_6(\text{Fe}, \text{Mn})$  crystal and show a round or near-rhombic shape (Figure 3 a-c). While, there also exists some hollows which are not fully enclosed by primary  $\text{Al}_6(\text{Fe}, \text{Mn})$  crystal and have irregular shapes, as shown in Figure 3d. It is also noted the outlines of the primary  $\text{Al}_6(\text{Fe}, \text{Mn})$  crystal has a strong faceted feature, but the interfaces between these internal hollows filled by  $\alpha$ -Al phase and the outside primary  $\text{Al}_6(\text{Fe}, \text{Mn})$  crystal that encloses them are curved and smooth. It means that the interfaces are not a certain crystal face, and thus the formation of these hollows is due to the incomplete growth of  $\text{Al}_6(\text{Fe}, \text{Mn})$  crystal.

Figure 4 illustrates several typical lath-like  $\text{Al}_6(\text{Fe}, \text{Mn})$  crystals. Hollows were also found in primary lath-like  $\text{Al}_6(\text{Fe}, \text{Mn})$  crystals. As shown in Figure 4a, they extend along the axial direction of  $\text{Al}_6(\text{Fe}, \text{Mn})$  lath to the top edge. However, a hollow can't traverse the whole  $\text{Al}_6(\text{Fe}, \text{Mn})$  lath. There also exists a solid  $\text{Al}_6(\text{Fe}, \text{Mn})$  part without hollow, as shown in Figure 4 b-d. while the length of solid  $\text{Al}_6(\text{Fe}, \text{Mn})$  parts is different. At the both ends of a solid part, two separate hollows are generated and then extended. It was also noted that the interfaces between the hollows and the  $\text{Al}_6(\text{Fe}, \text{Mn})$  crystal are also curved and smooth.

It was reported that Fe and Mn atoms in  $\text{Al}_6(\text{Fe}, \text{Mn})$  phase can substitute each other without changing the crystal structure [16]. Therefore, the composition of  $\text{Al}_6(\text{Fe}, \text{Mn})$  was also analysed by EDS. Table 1 shows the average Mn/Fe atomic ratio of 20  $\text{Al}_6(\text{Fe}, \text{Mn})$  particles in each experimental Al-Mg-Mn-Fe alloy. It was found that the Mn/Fe atomic ratio of  $\text{Al}_6(\text{Fe}, \text{Mn})$  phase decreases from 0.64 to 0.32, as the increase of Fe level in alloy from 0.5% to 2.0%. While, the composition change doesn't lead to morphological evolution. It was also noted that, in the 0.5Fe alloy, the atomic ratio of Mn/Fe is 1.33, which is much higher than that in  $\text{Al}_6(\text{Fe}, \text{Mn})$  phase (0.64). This difference indicates that lots of Mn atoms dissolve into  $\alpha$ -Al solid solution because of the high solubility of Mn in  $\alpha$ -Al. While, as the Fe level increases, the aforementioned difference becomes small in the 1.0Fe alloy and even nearly disappears in the 1.5Fe and the 2.0Fe alloys. It means that the addition of Fe can reduce the solubility of Mn in Al-Mg-Mn-Fe alloys, thus Mn is pushed to precipitate as  $\text{Al}_6(\text{Fe}, \text{Mn})$  phase.

In the Al-5Mg-0.6Mn-2.0Fe alloy, several large unregular particles (marked by A in Figure 5a) was also found. EDS results shows that this phase is different with the  $\text{Al}_6(\text{Fe}, \text{Mn})$  phase (marked by B in Figure 5a) and has an atomic ratio of Al/(Fe, Mn) of 3.36. Therefore, it is identified as  $\text{Al}_{13}(\text{Fe}, \text{Mn})_4$  phase. While, the amount of  $\text{Al}_{13}(\text{Fe}, \text{Mn})_4$  phase is so limited that it can't been detected by XRD. In the present work, the efforts would be focused on the dominant  $\text{Al}_6(\text{Fe}, \text{Mn})$  phase.

### 3.2 Formation of metastable $\text{Al}_6(\text{Fe}, \text{Mn})$ phase

Phase competition is a common phenomenon in Al-Fe and Al-Mn systems under high cooling rate, and has been intensively studied [17-20]. However, the competitive precipitation of stable and metastable (Fe,Mn)-rich phases in Al-Mg-Mn-Fe alloys has never been studied. To further understand the formation of  $\text{Al}_6(\text{Fe}, \text{Mn})$  phase, the cross section of the stable equilibrium phase diagram of Al-5Mg-0.6Mn-xFe alloys was calculated by Pandat software

in the present work. According to Figure 6a, eutectic  $\text{Al}_{13}\text{Fe}_4$  should exist in all experimental alloys. What's more, the only primary (Fe, Mn)-rich phase should be  $\text{Al}_{13}\text{Fe}_4$ . However, expect a few primary  $\text{Al}_{13}(\text{Fe}, \text{Mn})_4$  particles in the 2.0Fe alloy, all the eutectic and primary phases in the experimental alloys are  $\text{Al}_6(\text{Fe}, \text{Mn})$  phase. It means that there exists a competition between stable  $\text{Al}_{13}(\text{Fe}, \text{Mn})_4$  phase and metastable  $\text{Al}_6(\text{Fe}, \text{Mn})$  phase, and metastable  $\text{Al}_6(\text{Fe}, \text{Mn})$  phase wins by a landslide. Then, the metastable equilibrium phase diagram of the Al-5Mg-0.6Mn-xFe alloys were calculated, as shown in Figure 6b. It shows that the eutectic point locates at 1.86% Fe, which also doesn't match the observed fact that primary  $\text{Al}_6(\text{Fe}, \text{Mn})$  has already appeared in the 1.0 Fe alloy, as shown in Figure 1c. Based on above discussions, it can be concluded that the metastable  $\text{Al}_6(\text{Fe}, \text{Mn})$  phase formed in an undercooled melt under a non-equilibrium solidification process.

Which phase would be dominant in solidified microstructure is controlled by nucleation. From the view of thermodynamics, the simultaneous nucleation of both stable  $\text{Al}_{13}(\text{Fe}, \text{Mn})_4$  and metastable  $\text{Al}_6(\text{Fe}, \text{Mn})$  phases is possible in the experimental alloys. In this case, kinetic factors would play a critical role. Nucleation is actually a process during which solute atoms or clusters gather together to form embryos with critical nucleation radius. Therefore, diffusion has a great influence on nucleation. According to Malakhov's study [20], if the composition of a phases is close to the melt composition, then the precipitation of this particular phases is facilitated, because corresponding nucleation event does not require a long-range diffusion, which might be slow in supercooled melt. Table 2 shows the concentration of Fe and Mn elements in the experimental Al-5Mg-0.6Mn-xFe melts and  $\text{Al}_{13}(\text{Fe}, \text{Mn})_4$  and  $\text{Al}_6(\text{Fe}, \text{Mn})$  phases. Obviously, the compositions of the melt and  $\text{Al}_6(\text{Fe}, \text{Mn})$  are relatively close to each other. On the contrary,  $\text{Al}_{13}(\text{Fe}, \text{Mn})_4$  is so enriched with Fe and Mn that its composition is far away from melt compositions. Therefore, the formation of  $\text{Al}_6(\text{Fe}, \text{Mn})$  is favoured. On the other hand, several researches of liquid structure of Al-Fe melt also indicate that there exist  $\text{Al}_6\text{Fe}$  type clusters in melt, rather than  $\text{Al}_3\text{Fe}$  type cluster [21-24]. It provides the structural benefit for the formation of  $\text{Al}_6\text{Fe}$ , which has the almost same crystal structure with  $\text{Al}_6(\text{Fe}, \text{Mn})$ . Therefore, in the view of kinetic pathway, the metastable  $\text{Al}_6(\text{Fe}, \text{Mn})$  phase can be considered as an intermediate phase for final stable  $\text{Al}_{13}(\text{Fe}, \text{Mn})_4$  phase. Under equilibrium solidification condition, the intermediate metastable  $\text{Al}_6(\text{Fe}, \text{Mn})$  phase has a very short life and transforms to stable  $\text{Al}_{13}(\text{Fe}, \text{Mn})_4$  phase. However, under high cooling rate, the diffusion of solute atoms is limited, thus the life time of metastable  $\text{Al}_6(\text{Fe}, \text{Mn})$  phase is expanded, so that it can exist in solidified alloys as a

dominate phase. In Al-Fe alloys fabricated by mechanical alloying, metastable  $\text{Al}_6\text{Fe}$  was also found and can transformed into stable  $\text{Al}_{13}\text{Fe}_4$  phase during heat treatment process [25].

In the present work, many primary  $\text{Al}_6(\text{Fe}, \text{Mn})$  particles were observed. However, no primary  $\text{Al}_6\text{Fe}$  particle was found in the existing literatures, although  $\text{Al}_6\text{Fe}$  eutectic phase is common in rapid solidified alloys [26,27]. A series of Al-5Mg-xFe alloys (x=0.5, 1.0, 1.5 and 2.0) were also prepared under the same cooling conditions. From the SEM micrograph and XRD patterns shown in Figure 7, it is found that the only Fe-rich phase in Al-Mg-Fe alloys is stable  $\text{Al}_{13}\text{Fe}_4$  phase, rather than metastable  $\text{Al}_6\text{Fe}$  phase. Therefore, by comparing the existing phases in Al-Mg-Fe and Al-Mg-Mn-Fe alloys, it can be concluded that Mn plays a critical role in the formation of metastable phase. The existence of metastable phase is ensured by the energy barrier in the path of transformation from metastable phase to stable phase in the system. Our present results indicate that the addition of Mn enlarges the energy barrier in the  $\text{Al}_6(\text{Fe}, \text{Mn}) \rightarrow \text{Al}_{13}(\text{Fe}, \text{Mn})_4$  transformation path. However, the study on (1) the liquid structure of Al-Fe-Mn melt and (2) activation energy for AlFeMn phase formation is still rare up to now, it is different to draw a clear atom-scale perspective for the role of Mn.

### 3.3 3D morphology of $\text{Al}_6(\text{Fe}, \text{Mn})$ phase

To clearly reveal the morphologies of  $\text{Al}_6(\text{Fe}, \text{Mn})$  phase, a 15 vol% HCl water solution was applied to extract these intermetallic particles by completely removing the Al-Mg matrix. Although two shapes (rhombus and lath) are observed in 2D sections (Figures 1, 3 and 4), Figures 8 and 9 show that all primary  $\text{Al}_6(\text{Fe}, \text{Mn})$  crystals have only one 3D morphology, i.e. quadrangular prism. The rhombus and lath shapes are in fact the 2D polygonal outlines of quadrangular prism cut at random angles. As shown in Figure 8, most  $\text{Al}_6(\text{Fe}, \text{Mn})$  quadrangular prisms are elongated along a direction, while a few particles also have large side faces, showing a plate-like morphology (Figure 8b). Hollows are found in almost each primary  $\text{Al}_6(\text{Fe}, \text{Mn})$  prism. In most cases, hollows are inside of the  $\text{Al}_6(\text{Fe}, \text{Mn})$  prism and can be observed only at the end face, as shown in Figure 8c. While, there also exist some hollows which invade side faces, as shown in Figure 8d. Figure 9 shows the morphologies of primary  $\text{Al}_6(\text{Fe}, \text{Mn})$  phase along the cross direction. It was found the end faces of primary  $\text{Al}_6(\text{Fe}, \text{Mn})$  prisms have two shapes, including rhombus and rectangle. Therefore, the morphology characteristics of primary  $\text{Al}_6(\text{Fe}, \text{Mn})$  phase in the experimental Al-Mg-Mn-Fe alloys take on rhombic prism and rectangular prism.

Figure 10 shows the 3D morphologies of eutectic  $\text{Al}_6(\text{Fe}, \text{Mn})$  phase. Similar with the primary  $\text{Al}_6(\text{Fe}, \text{Mn})$  phase, the eutectic  $\text{Al}_6(\text{Fe}, \text{Mn})$  phase also have a morphology of quadrangular prism. From the crystallographic investigation results in Figure 10, it seems that eutectic  $\text{Al}_6(\text{Fe}, \text{Mn})$  phase prefer to rhombic prism. However, the rectangular prism can't be excluded because eutectic  $\text{Al}_6(\text{Fe}, \text{Mn})$  phase is too small (200-500 nm in cross section) to accurately identify the similar rhombus and rectangle shapes. It was also noted that all eutectic  $\text{Al}_6(\text{Fe}, \text{Mn})$  prisms have no hollow, which is distinguished from the primary  $\text{Al}_6(\text{Fe}, \text{Mn})$  prism.

### 3.4 Growth mechanism of $\text{Al}_6(\text{Fe}, \text{Mn})$ phase

During the crystal growth process, the faster growing faces tend to disappear at last, thus have less probability of appearing in the final morphology of the crystal as compared to the slower growing ones. According to the Bravais-Friedel-Donnay-Harker law (BFDH) law [28], for a crystal with equilibrium morphology, the growth rate of a given  $\{hkl\}$  face is inversely proportional to the interplanar distance  $d_{hkl}$  after taking into account the extinction conditions of the crystal symmetry. Figure 11 shows the crystal structure of  $\text{Al}_6(\text{Fe}, \text{Mn})$  phase. It has an orthorhombic structure with  $a=0.7498$  nm,  $b=0.6495$  nm,  $c=0.8837$  nm (when atomic ratio of Fe to Mn is 1). The space group of  $\text{Al}_6(\text{Fe}, \text{Mn})$  crystal is  $\text{Cmcm}$  (63). For this crystal, the interplanar distance for a given  $\{h k l\}$  face ( $h+k \neq 2n$ ) should be calculated as  $\{2h \ 2k \ 2l\}$ . Table 3 shows the morphological importance (MI) of orthorhombic  $\text{Al}_6(\text{Fe}, \text{Mn})$  crystal faces according to BFDH law. MI of a habit ( $hkl$ ) face is a measure of the probability of that face relative to the other faces appearing in the morphology. The greater the MI, the larger the probability. Table 3 also lists the simple forms corresponding to these morphologically importance faces. A crystal form is a set of crystal faces that have the same arrangement of atoms and are related to each other by symmetry. The number of faces contained in a form is named as multiplicity. Here, it should be noted that, in crystallography, the  $\{110\}$  form rhombic prism only refers to four side faces of an enclosed geometrical rhombic prisms. Therefore, the multiplicity of  $\{110\}$  form is only 4.

The crystal morphology can be considered as a combination of one or several forms. Both rectangular prism and rhombic prism of  $\text{Al}_6(\text{Fe}, \text{Mn})$  crystal observed in the Al-Mg-Mn-Fe alloys have 6 faces. Thus, according to Table 2, there exist four possible configurations: (i)  $\{110\}+\{002\}$ , (ii)  $\{110\}+\{200\}$ , (iii)  $\{110\}+\{020\}$ , (iv)  $\{002\}+\{200\}+\{020\}$ . Among them, only the last one constitutes a rectangular prism. While, all the other three can form rhombic

prism. So, a further experimental identification is necessary to reveal the detailed morphology of rhombic prism.

Figure 12 shows a series of maps generated from the raw data of an extracted  $\text{Al}_6(\text{Fe}, \text{Mn})$  rhombic prism by EBSD analysis. As shown in Figure 12a, the side face (marked as A) of this  $\text{Al}_6(\text{Fe}, \text{Mn})$  prism is parallel to the surface of sample stage. So, this side face just corresponds to the central point in scattered pattern map (Figure 12b) and pole figure map (Figure 12c), and then identified as (110). It is also confirmed by the inverse pole figure (normal direction, ND) (Figure 12d). Therefore, the four side faces of this rhombic prism are belonging to {110}. The end face can be identified by inverse pole figure. However, the longitudinal direction of this prism is not parallel to rolling direction (RD) and ND, as shown in Figure 12a. It is not convenient to analysis the miller index of end face by raw inverse pole figure (the left part of Figure 12d). So, a new inverse pole figure was simulated by TEAM software after rotating sample by  $45^\circ$  round ND, as shown in the right part of Figure 12d. In this case, the longitudinal direction of this prism is parallel to RD, which was identified as [001]. Thus, it can be concluded the end face is {002}. In other words, the rhombic prism is constituted by {110} and {002} forms. It is noticed that {110} and {002} are top 2 morphologically important faces according to Table 3. Therefore, the rhombic prism bounded by {110} and {002} are the equilibrium morphology of  $\text{Al}_6(\text{Fe}, \text{Mn})$  phase. While, the rectangular prism bounded by {002}, {200} and {020} is a growth morphology, which was affected by growth conditions (such as impurity atoms) and deviated from the equilibrium morphology.

After determining the miller index of exposed faces, the growth mechanism of  $\text{Al}_6(\text{Fe}, \text{Mn})$  crystal and the formation of inside hollows were studied, as shown in Figure 13. Liquid melt is composed mainly of atomic clusters and a few free atoms, and microsegregation easily exists in the melt [29,30]. As the solidification of melt starts, these atomic clusters and microsegregation can form a seed crystal through fluctuations in structure and energy [31]. To gain the minimum free energy, the initial seed crystal presents a spherical (or round) morphology. When the seed crystal grows and exceeds a critical size, it becomes unstable. At the initial stage of faceted crystal growth, dendritic plays an important role. A few hillocks generate on the surface of seed  $\text{Al}_6(\text{Fe}, \text{Mn})$  crystal and rapidly grows to first branches along the its first preferential growth directions, as shown in Figure 13b. Due to the complicated crystal structure of  $\text{Al}_6(\text{Fe}, \text{Mn})$ , it is not easy to determine the preferential growth directions

by only analysing the crystal structure. While, it can be reduced from the intermediate  $\text{Al}_6(\text{Fe}, \text{Mn})$  morphology shown in Figure 13c that its first preferential growth directions are  $[001]$ ,  $[100]$  and  $[010]$ . Meanwhile, new secondary branches would generate on the first branches and grows in the interspace between first branches. Subsequently,  $\text{Al}_6(\text{Fe}, \text{Mn})$  has a strong intrinsic faceting tendency. Therefore, the  $\{110\}$  and  $\{002\}$  faceted faces, which has the lowest surface free energy, appear at the top of existing branches, as shown in Figure 13c. Then  $\text{Al}_6(\text{Fe}, \text{Mn})$  grows by the deposition of atomic clusters (and some atoms) to form new layers on  $\{110\}$  and  $\{002\}$  faceted faces in a two-dimensional lateral growth manner. As the result, these adjacent branches will join each other and form a small solid rhombic prism bounded by six  $\{110\}$  and  $\{002\}$  faces, as show in Figure 13d.

In the following growth stage, the exposed faceted  $\{110\}$  and  $\{002\}$  faces would further grow. While, according to Table 3,  $\{002\}$  has a higher growth rate than  $\{110\}$ , therefore the solid rhombic prism is elongated along  $[001]$  direction. The subsequent formation of hollow inside prism indicates that the crystal growth process is determined by volume-diffusion. At this stage, the transport of solute atoms is important, especially for the faster growing  $\{002\}$  faces. Compared with the diffusion in the areas adjacent to edges, the diffusion in the central area of  $\{002\}$  faces is relatively difficult. Therefore, the supplement of solute atoms and the ejection of impurities expelled from crystalized  $\text{Al}_6(\text{Fe}, \text{Mn})$  crystal are relatively slow. These two factors will retard the  $\text{Mg}_2\text{Si}$  growth in central areas of  $\{002\}$  faces, leading to the formation of hollows inside primary  $\text{Al}_6(\text{Fe}, \text{Mn})$  prism, as shown in Figure 13 e and f. While, due to the small volume of eutectic  $\text{Al}_6(\text{Fe}, \text{Mn})$  crystal, the effect of volume-diffusion is too weak to form hollows. Thus, eutectic  $\text{Al}_6(\text{Fe}, \text{Mn})$  crystal is still solid, as show in Figure 13g. The rectangular  $\text{Al}_6(\text{Fe}, \text{Mn})$  prism has a similar growth process. While, its  $\{110\}$  faces are restrained by some kinetic factors, and replaced by  $\{200\}$  and  $\{020\}$  as the exposed side faces of prism.

#### **4. Conclusions**

In the present work, the formation, 3D morphologies and growth mechanism of metastable  $\text{Al}_6(\text{Fe}, \text{Mn})$  phase in HPDC Al-Mg alloys were investigated. The main results are summarized as follows:

- (1) The addition of Mn suppresses the  $\text{Al}_6(\text{Fe}, \text{Mn}) \rightarrow \text{Al}_{13}(\text{Fe}, \text{Mn})_4$  transformation, promotes the formation of metastable  $\text{Al}_6(\text{Fe}, \text{Mn})$  phase in HPDC Al-Mg-Mn-Fe

alloys. Besides, the average Mn/Fe atomic ratio of Al<sub>6</sub>(Fe, Mn) phase also decrease as the Mn/Fe atomic ratio of melt decreases.

- (2) The Al<sub>6</sub>(Fe, Mn) phase in HPDC Al-Mg-Mn-Fe alloys have two 3D morphologies: rhombic prism and rectangular prism. The rhombic prism (equilibrium morphology) is bounded by four {110} and two {002} faces, while the rectangular prism (growth morphology) is bounded by two {002}, two {200} and two {020} faces. The primary Al<sub>6</sub>(Fe, Mn) phase has inside hollows, while eutectic one is small and solid.
- (3) At the initial growth stage of Al<sub>6</sub>(Fe, Mn) phase, dendritic growth along preferred directions plays an important role. Then, Al<sub>6</sub>(Fe, Mn) has a strong intrinsic faceting tendency and develops to be a solid prism. Subsequently, volume-diffusion restrains the growth of central area of end faces of Al<sub>6</sub>(Fe, Mn) prism, leading to the formation of hollows inside primary Al<sub>6</sub>(Fe, Mn) phase. While, the small eutectic Al<sub>6</sub>(Fe, Mn) phase is not affected by volume-diffusion and remains a solid morphology.

## Acknowledgements

Financial support from Jaguar Range Rover (JLR) [grant number R33232] is gratefully acknowledged.

## References

- [1] S. Ji, W. Yang, F. Gao, D. Watson, Z. Fan, Effect of iron on the microstructure and mechanical property of Al-Mg-Si-Mn and Al-Mg-Si diecast alloys, *Mater. Sci. Eng. A.* 564 (2013) 130-139.
- [2] H. Yang, D. Watson, Y. Wang, S. Ji, Effect of nickel on the microstructure and mechanical property of die-cast Al-Mg-Si-Mn alloy, *J. Mater. Sci.* 49 (2014) 8412-8422.
- [3] P. Skjerpe, Intermetallic phases formed during DC-casting of an Al-0.25Fe-0.13Si alloy, *Metall. Mater. Trans. A.* 18 (1987) 189-200.
- [4] S. Shivkumar, L. Wang, D. Apelian, Molten metal processing of advanced cast aluminum alloys, *JOM J. Miner. Met. Mater. Soc.* 43 (1991) 26-32.
- [5] X. Cao, J. Campbell, Precipitation of primary intermetallic compounds in liquid Al-11.5Si-0.4Mg alloy, *Int. J. Cast Met. Res.* 13 (2000) 175-184.
- [6] J.R. Davis, *Aluminum and aluminum alloys*, ASM international, 1993.
- [7] L. Zhang, J. Gao, L.N.W. Damoah, D.G. Robertson, Removal of iron from aluminum: a review, *Miner. Process. Extr. Metall. Rev.* 33 (2012) 99-157.
- [8] N.A. Belov, V.S. Zolotarevskii, Optimization of the composition of low-silicon silumin in

- order to increase mechanical properties in the castable state, *Russ. J. Non-Ferrous Met.* 42 (2001) 37-47.
- [9] J.R. Davis, *Alloying: understanding the basics*, ASM International, 2001.
- [10] Y. Liu, L. Luo, C. Han, L. Ou, J. Wang, C. Liu, Effect of Fe, Si and cooling rate on the formation of Fe-and Mn-rich intermetallics in Al-5Mg-0.8Mn alloy, *J. Mater. Sci. Technol.* 32 (2016) 305-312.
- [11] Y. Liu, Y. Sun, L. Zhang, Y. Zhao, J. Wang, C. Liu, Microstructure and mechanical properties of Al-5Mg-0.8Mn alloys with various contents of Fe and Si cast under near-rapid cooling, *Metals.* 7 (2017) 428.
- [12] Y. Liu, G. Huang, Y. Sun, L. Zhang, Z. Huang, J. Wang, C. Liu, Effect of Mn and Fe on the formation of Fe-and Mn-rich intermetallics in Al-5Mg-Mn alloys solidified under near-rapid cooling, *Materials.* 9 (2016) 88.
- [13] P. Yang, O. Engler, H. J. Klaar, Orientation relationship between Al<sub>6</sub>Mn precipitates and the Al matrix during continuous recrystallization in Al-1.3%Mn, *J. Appl. Crystallogr.* 32 (1999) 1105-1118.
- [14] B.O. Kong, S.W. Nam, Investigation of growth mechanism and orientation relationship of Mn-dispersoid in an Al-Zn-Mg-Mn alloy, *Mater. Lett.* 28 (1996) 385-391.
- [15] B.O. Kong, J.I. Suk, S.W. Nam, Identification of Mn-dispersoid in Al-Zn-Mg-Mn alloy, *J. Mater. Sci. Lett.* 15 (1996) 763-766.
- [16] Y.J. Li, W.Z. Zhang, K. Marthinsen, Precipitation crystallography of plate-shaped Al<sub>6</sub>(Mn, Fe) dispersoids in AA5182 alloy, *Acta Mater.* 60 (2012) 5963-5974.
- [17] P. Gilgien, A. Zryd, W. Kurz, Microstructure selection maps for Al-Fe alloys, *Acta Metall. Mater.* 43 (1995) 3477-3487.
- [18] C.M. Allen, K.A.Q. O'reilly, B. Cantor, P. V Evans, Intermetallic phase selection in 1XXX Al alloys, *Prog. Mater. Sci.* 43 (1998) 89-170.
- [19] J.A. Juarez-Islas, D.H. Warrington, H. Jones, Formation of stable and metastable phases in Al-Mn alloys by the use of a gravity chill casting technique, *J. Mater. Sci.* 24 (1989) 2076-2080.
- [20] D. V Malakhov, D. Panahi, M. Gallerneault, On the formation of intermetallics in rapidly solidifying Al-Fe-Si alloys, *Calphad.* 34 (2010) 159-166.
- [21] P.J. Black, J.A. Cundall, The structure of liquid aluminum-iron alloys, *Acta Crystallogr.* 20 (1966) 417-424.
- [22] T. Egami, The atomic structure of aluminum based metallic glasses and universal criterion for glass formation, *J. Non. Cryst. Solids.* 205 (1996) 575-582.
- [23] J. Qin, X. Bian, W. Wang, J. Ma, C. Xu, Pre-peak on the structure factor of liquid hypoeutectic Al-Fe alloy, *Chinese Sci. Bull.* 43 (1998) 1219-1224.
- [24] J. Qin, X. Bian, W. Wang, S.I. Sijusarenko, J. Ma, C. Xu, Micro-inhomogeneous structure of liquid Al-Fe alloys, *Sci. China Ser. E Technol. Sci.* 41 (1998) 182-187.

- [25] X.P. Niu, A. Mulaba-Bafubiandi, L. Froyen, L. Delaey, C. Peytour, Mössbauer study of phase formation in mechanically alloyed Al-Fe and Al-Fe-Mn powders, *Scr. Metall. Mater.* 31 (1994) 1157-1162.
- [26] R.F. Cochrane, S.B. Newcomb, P. V Evans, A.L. Greer, Microstructural development in drop-tube processed Al-8wt.% Fe, *Key Eng. Mater.*, Trans Tech Publ, 38 (1990) 21-42.
- [27] R.F. Cochrane, P. V Evans, A.L. Greer, Competitive growth analysis of phase formation in Al-8wt.% Fe, *Mater. Sci. Eng. A.* 133 (1991) 803-806.
- [28] J.H. Donnay, D. Harker, A new law of crystal morphology extending the law of Bravais, *Am. Miner.* 22 (1937) 446-467.
- [29] B. Sadigh, M. Dzugutov, S.R. Elliott, Vacancy ordering and medium-range structure in a simple monatomic liquid, *Phys. Rev. B.* 59 (1999) 1-4.
- [30] W. Wang, X. Bian, J. Qin, S.I. Syliusarenko, The atomic-structure changes in Al-16Si alloy above the liquidus, *Metall. Mater. Trans. A.* 31 (2000) 2163-2168.
- [31] H. Chen, F. Zu, J. Chen, L. Zou, G. Ding, Z. Huang, The effect of melt overheating on the melt structure transition and solidified structures of Sn-Bi40 alloy, *Sci. China Ser. E Technol. Sci.* 51 (2008) 1402-1408.

Figure 1. Backscattered SEM micrographs showing the microstructures of the Al-5Mg-0.6Mn-xFe alloys: (a, b) x=0.5, (c, d) x=1.0, (e) x=1.5 and (f) x=2.0.

Figure 2. XRD patterns of the Al-5Mg-0.6Mn-xFe alloys (x=0, 0.5, 1.0, 1.5 and 2.0).

Figure 3. SEM micrographs showing the four-typical rhombic Al<sub>6</sub>(Fe, Mn) crystals with hollows in the as-cast Al-5Mg-0.6Mn-2.0Fe alloys.

Figure 4. SEM micrographs showing the typical lath-like Al<sub>6</sub>(Fe, Mn) crystals with hollows in the as-cast Al-5Mg-0.6Mn-2.0Fe alloys.

Figure 5. (a) Magnified backscattered SEM micrograph of the Fe-rich phase in the Al-5Mg-0.6Mn-2.0Fe alloy and (b) corresponding EDS results.

Figure 6. The cross section of the stable (a) and metastable (b) equilibrium phase diagram of the Al-5Mg-0.6Mn-xFe alloys calculated by Pandat software.

Figure 7. (a) Backscattered SEM micrograph of the Al-5Mg-2.0Fe alloy, and (b) XRD patterns of the Al-5Mg-xFe alloys (x=0, 0.5, 1.0, 1.5 and 2.0).

Figure 8. SEM micrographs showing the 3D morphologies (longitudinal direction) of primary Al<sub>6</sub>(Fe, Mn) phase in the as-cast Al-5Mg-0.6Mn-2.0Fe alloys.

Figure 9. SEM micrographs showing the 3D morphologies (cross direction) of primary Al<sub>6</sub>(Fe, Mn) phase in the as-cast Al-5Mg-0.6Mn-2.0Fe alloys.

Figure 10. SEM micrographs showing the 3D morphologies of divorced eutectic Al<sub>6</sub>(Fe, Mn) phase in the as-cast Al-5Mg-0.6Mn-2.0Fe alloys.

Figure 11. Crystal structure of Al<sub>6</sub>(Fe, Mn) phase.

Figure 12. Various maps generated from same EBSD point analysis to reveal the crystallographic feature of Al<sub>6</sub>(Fe, Mn) crystal, (a) SEM image, (b) scattered pattern map, (c) pole figure (PF) map, and (d) inverse pole figure (IPF) map.

Figure 13. Schematic of the growth process of prism Al<sub>6</sub>(FeMn) crystal bounded by {110} and {002}.

Table 1. The actual average Mn/Fe atomic ratios of the Al<sub>6</sub>(Fe, Mn) phase in the Al-5Mg-0.6Mn-xFe alloys

Table 2. Concentration of Fe and Mn elements in the experimental Al-5Mg-0.6Mn-xFe alloys and the Al<sub>13</sub>(Fe, Mn)<sub>4</sub> and Al<sub>6</sub>(Fe, Mn) phases

Table 3. Morphologically important (MI) faces of the orthorhombic Al<sub>6</sub>(Fe, Mn) crystal calculated by BFDH law and corresponding simple forms

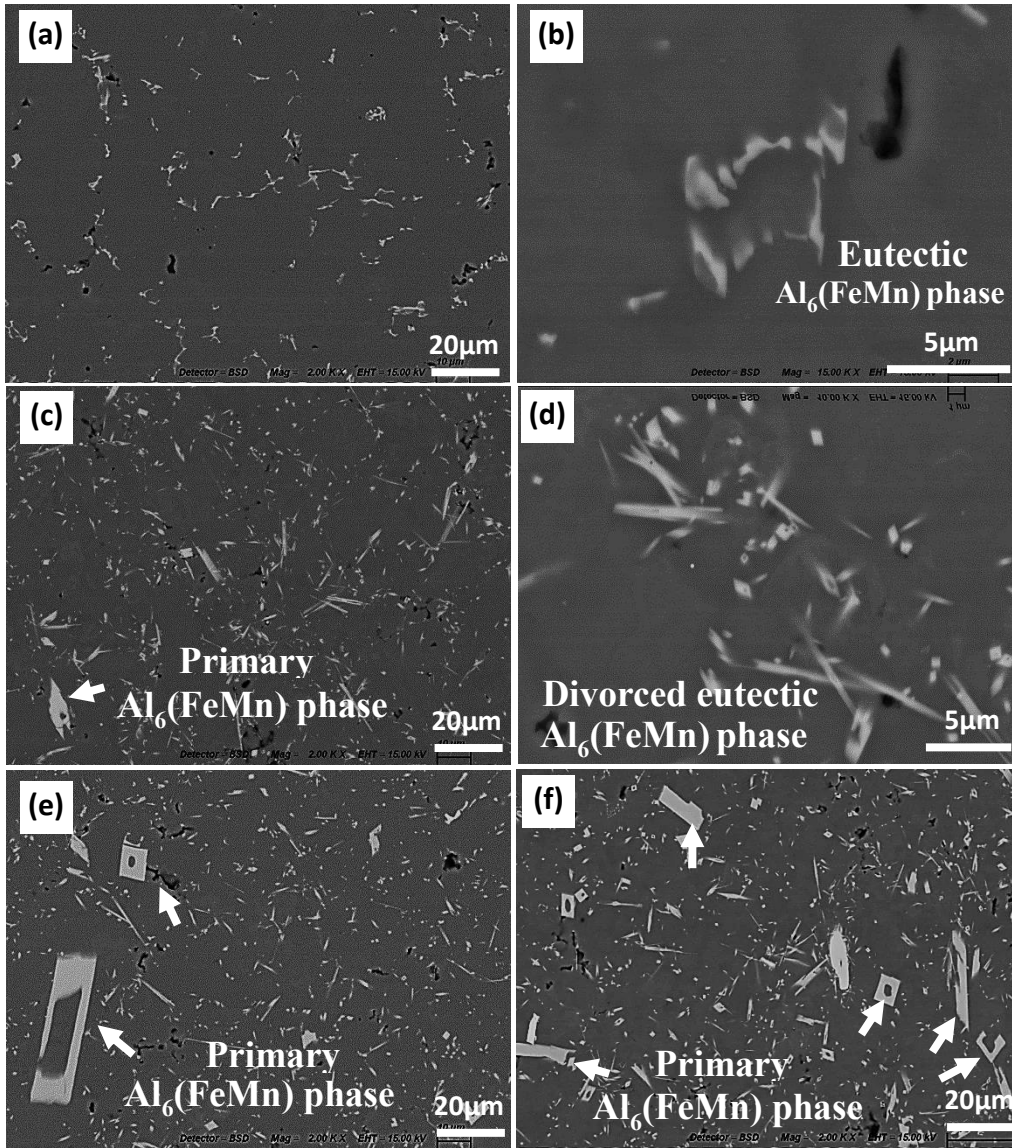


Figure 1. Backscattered SEM micrographs showing the microstructures of the Al-5Mg-0.6Mn-xFe alloys: (a, b) x=0.5, (c, d) x=1.0, (e) x=1.5 and (f) x=2.0.

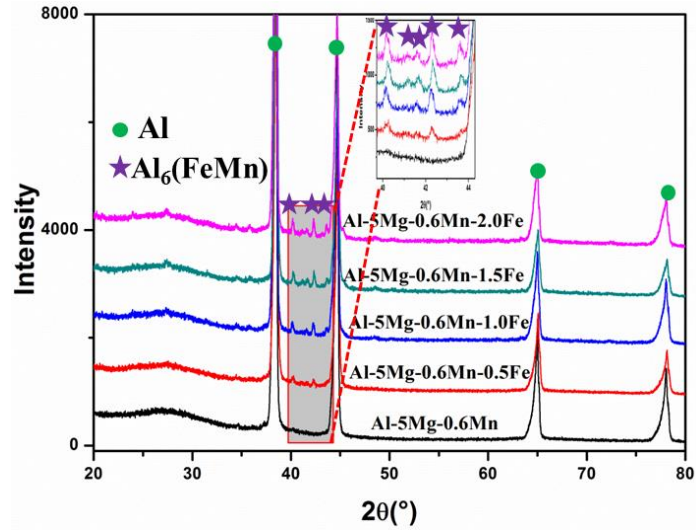


Figure 2. XRD patterns of the Al-5Mg-0.6Mn-xFe alloys (x=0, 0.5, 1.0, 1.5 and 2.0).

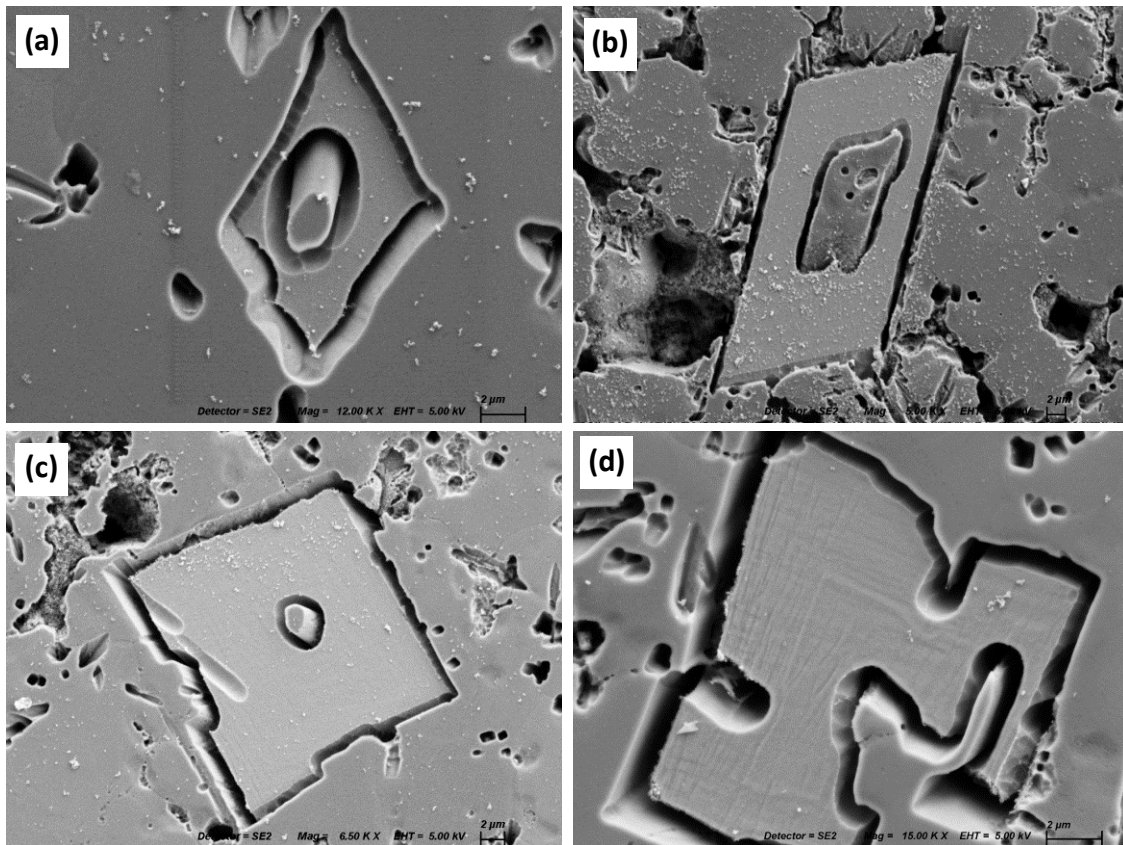


Figure 3. SEM micrographs showing the four-typical rhombic Al<sub>6</sub>(Fe, Mn) crystals with hollows in the as-cast Al-5Mg-0.6Mn-2.0Fe alloys.

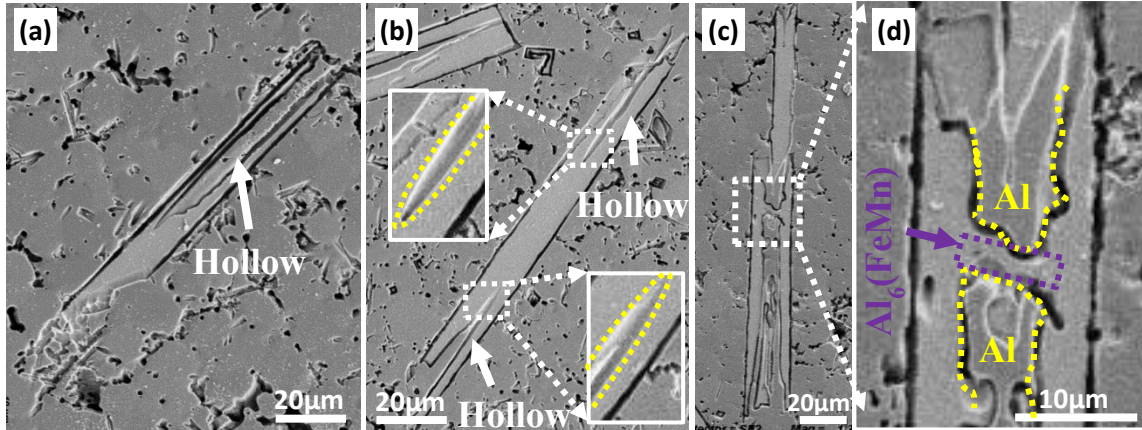


Figure 4. SEM micrographs showing the typical lath-like  $\text{Al}_6(\text{Fe}, \text{Mn})$  crystals with hollows in the as-cast Al-5Mg-0.6Mn-2.0Fe alloys.

Table 1. The actual average Mn/Fe atomic ratios of the  $\text{Al}_6(\text{Fe}, \text{Mn})$  phase in the Al-5Mg-0.6Mn-xFe alloys

Al-5Mg-0.6Mn-xFe*	0.5Fe	1.0Fe	1.5Fe	2.0Fe
Mn/Fe in the alloy	1.33	0.55	0.39	0.31
Mn/Fe in the $\text{Al}_6(\text{Fe}, \text{Mn})$ phase	0.64	0.43	0.38	0.32

\* Actual Fe contents were measured as 0.46, 1.10, 1.58 and 1.95, respectively. Actual Mn contents were measured as  $0.60 \pm 0.03$ .

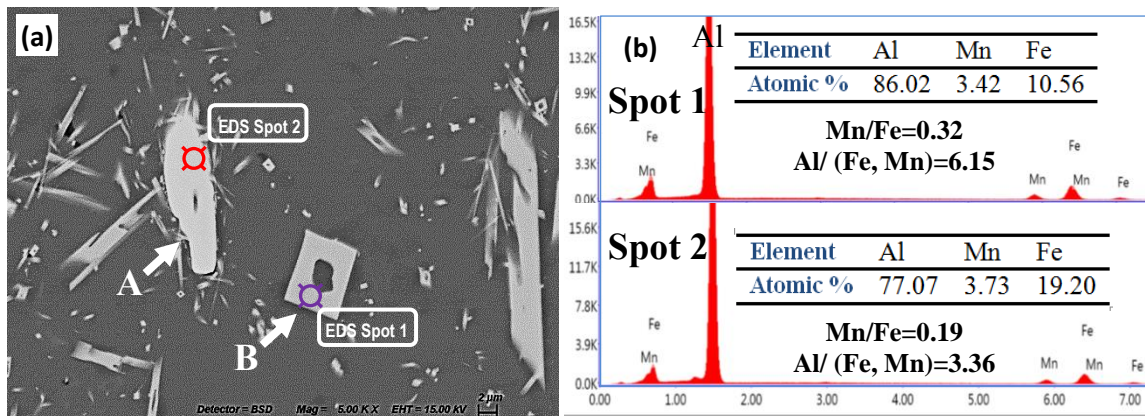


Figure 5. (a) Magnified backscattered SEM micrograph of the Fe-rich phase in the Al-5Mg-0.6Mn-2.0Fe alloy and (b) corresponding EDS results.

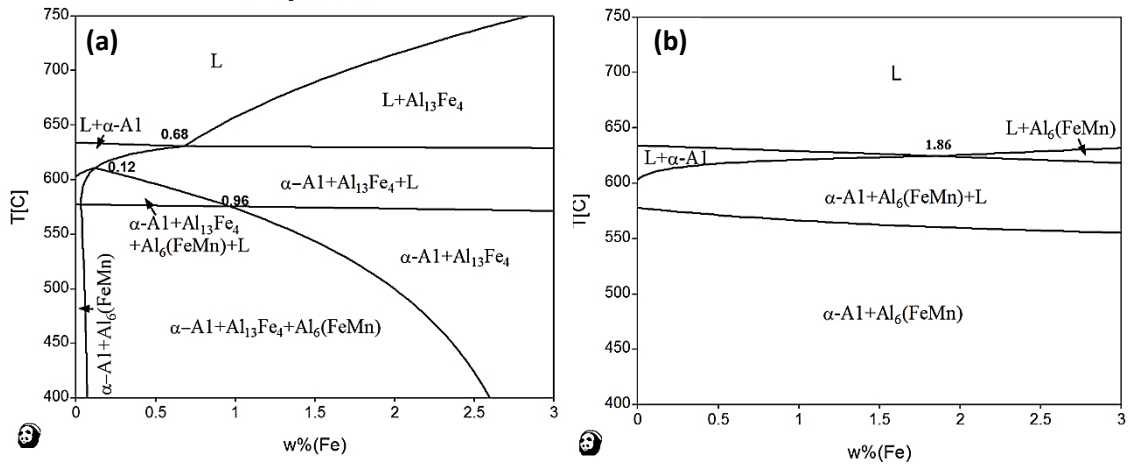


Figure 6. The cross section of the stable (a) and metastable (b) equilibrium phase diagram of the Al-5Mg-0.6Mn-xFe alloys calculated by Pandat software.

Table 2. Concentration of Fe and Mn elements in the experimental Al-5Mg-0.6Mn-xFe alloys and the  $Al_{13}(Fe, Mn)_4$  and  $Al_6(Fe, Mn)$  phases

Alloy/ Phase	Al-5Mg-0.6Mn-xFe				$Al_6(Fe, Mn)$	$Al_{13}(Fe, Mn)_4$
	0.5Fe	1.0Fe	1.5Fe	2.0Fe		
Mn and Fe (at.%)	0.52	0.83	1.07	1.25	14.29	23.53

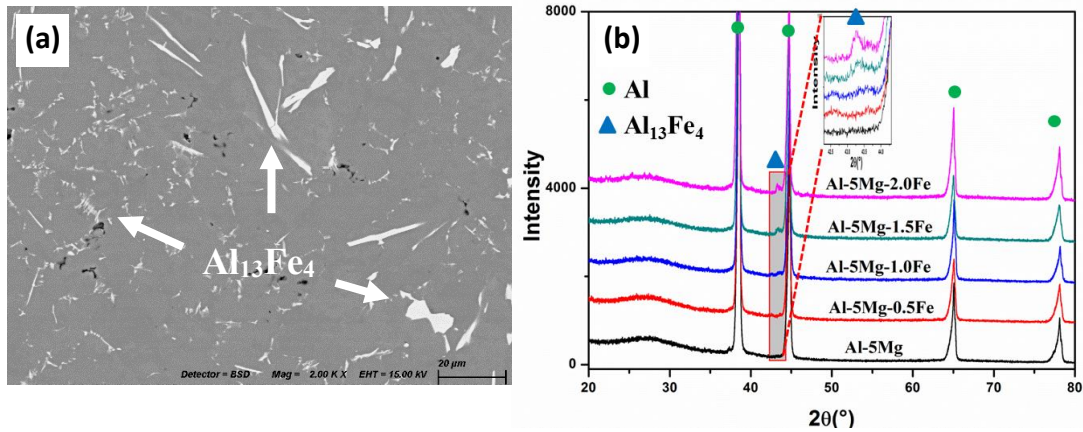


Figure 7. (a) Backscattered SEM micrograph of the Al-5Mg-2.0Fe alloy, and (b) XRD patterns of the Al-5Mg-xFe alloys (x=0, 0.5, 1.0, 1.5 and 2.0).

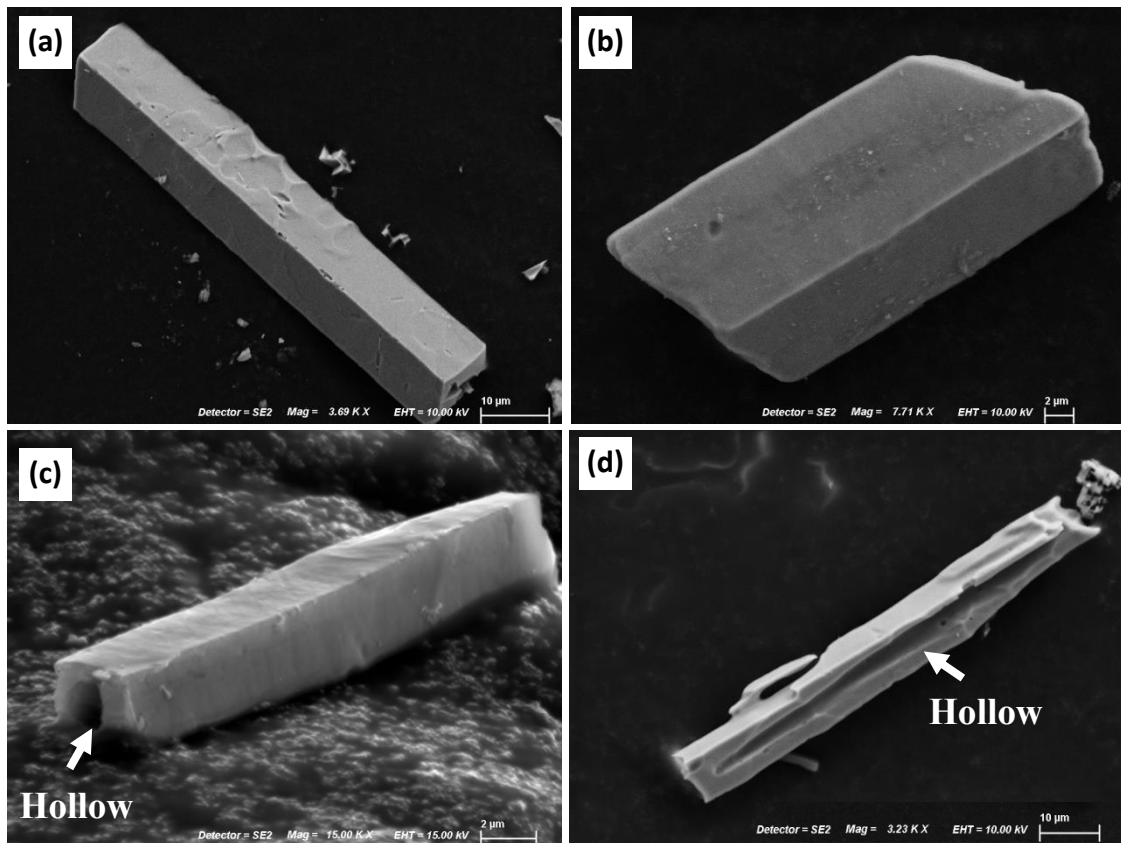


Figure 8. SEM micrographs showing the 3D morphologies (longitudinal direction) of primary  $Al_6(Fe, Mn)$  phase in the as-cast Al-5Mg-0.6Mn-2.0Fe alloys.

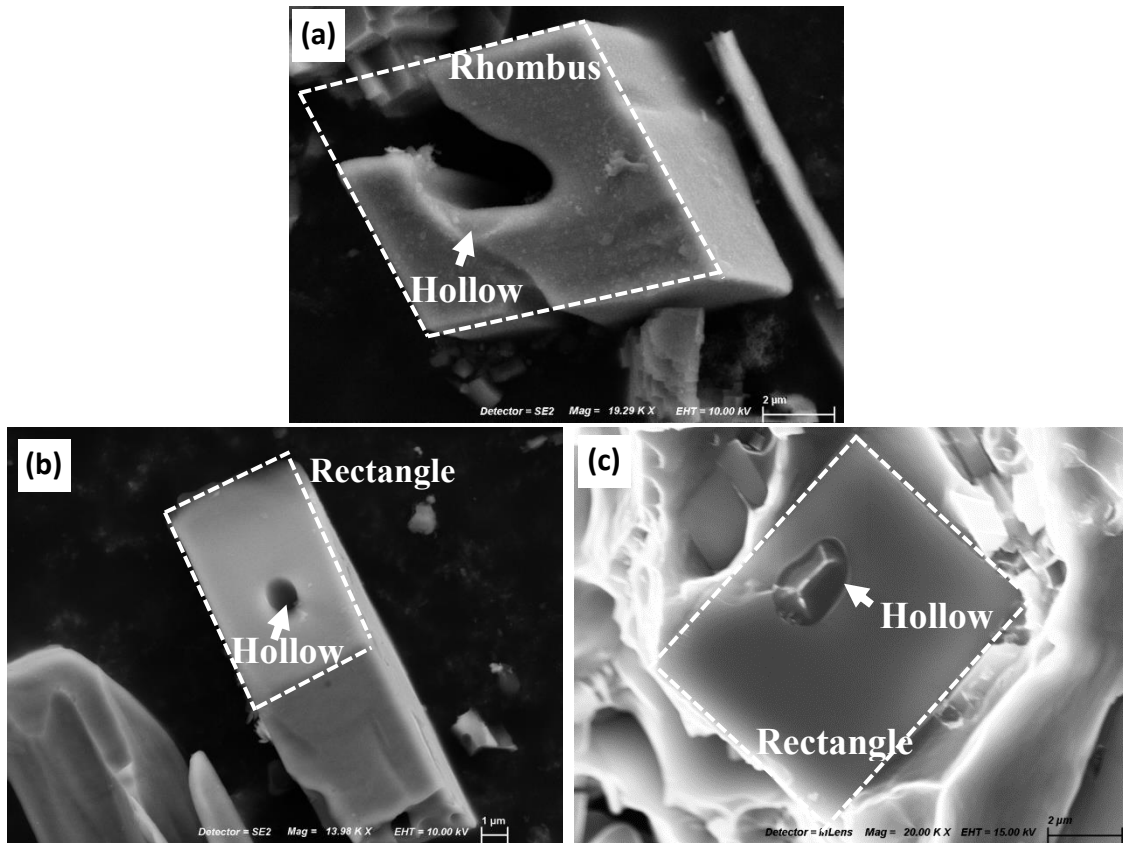


Figure 9. SEM micrographs showing the 3D morphologies (cross direction) of primary  $Al_6(Fe, Mn)$  phase in the as-cast Al-5Mg-0.6Mn-2.0Fe alloys.

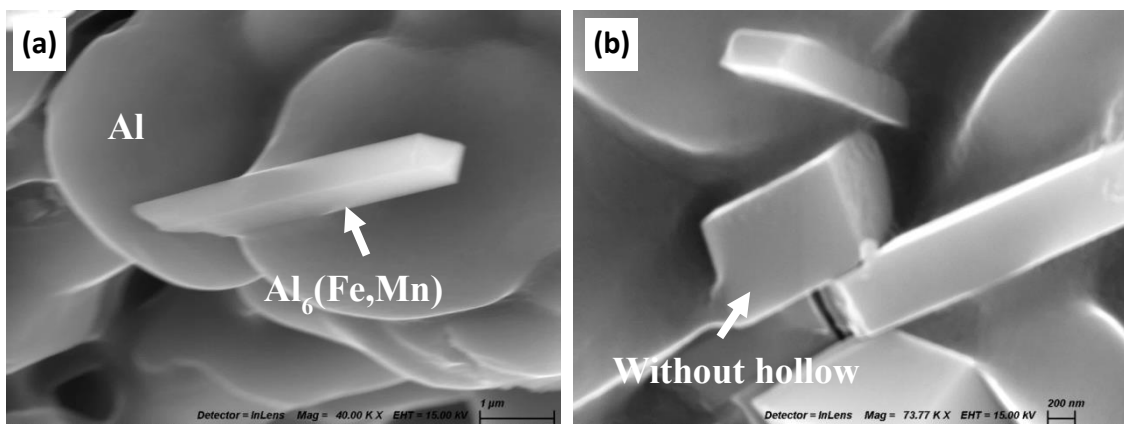


Figure 10. SEM micrographs showing the 3D morphologies of divorced eutectic  $Al_6(Fe, Mn)$  phase in the as-cast Al-5Mg-0.6Mn-2.0Fe alloys.

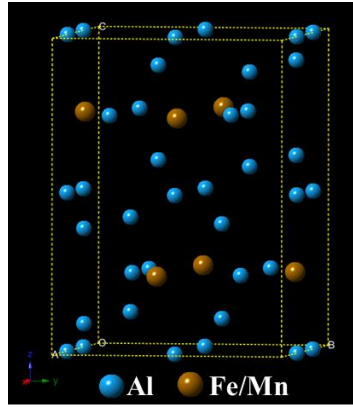


Figure 11. Crystal structure of  $\text{Al}_6(\text{Fe}, \text{Mn})$  phase.

Table 3. Morphologically important (MI) faces of the orthorhombic  $\text{Al}_6(\text{Fe}, \text{Mn})$  crystal calculated by BFDH law and corresponding simple forms

MI	Face (hkl)	d/nm	Multiplicity	Simple form
1	{110}	0.4927	4	Rhombic prism
2	{002}	0.4436	2	Pinacoids
3	{111}	0.4307	8	Rhombic pyramid
4	{200}	0.3778	2	Pinacoids
5	{112}	0.3297	8	Rhombic pyramid
6	{020}	0.3250	2	Pinacoids

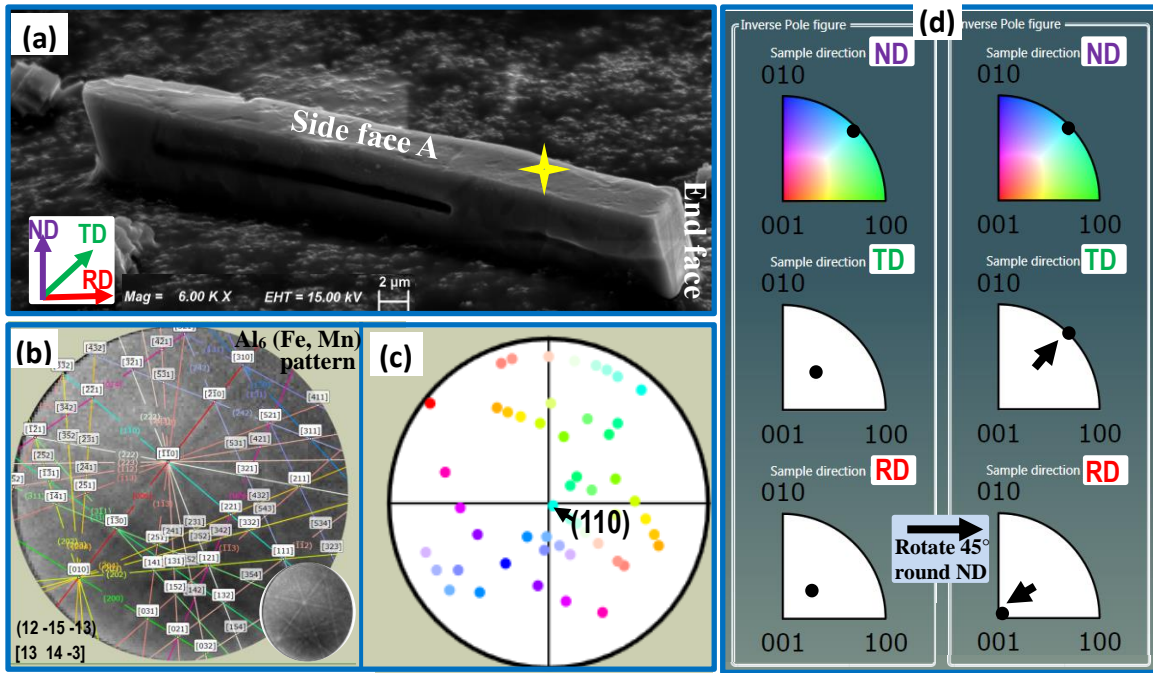


Figure 12. Various maps generated from same EBSD point analysis to reveal the crystallographic feature of  $\text{Al}_6(\text{Fe, Mn})$  crystal, (a) SEM image, (b) scattered pattern map, (c) pole figure (PF) map, and (d) inverse pole figure (IPF) map.

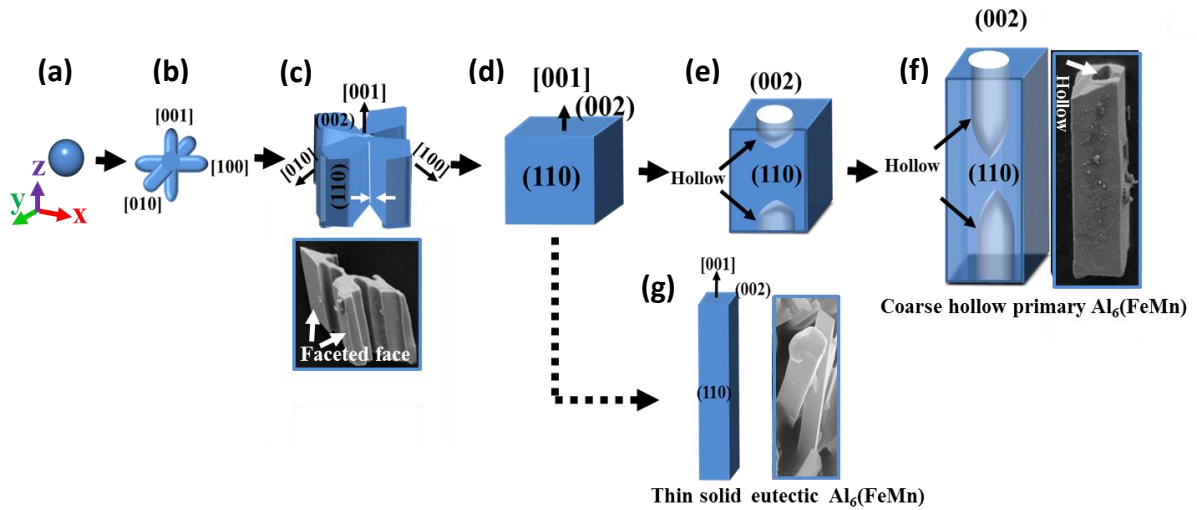


Figure 13. Schematic of the growth process of prism  $\text{Al}_6(\text{FeMn})$  crystal bounded by  $\{110\}$  and  $\{002\}$ .